A Targeted Quadrature Framework for Simulating Large-Scale 3D Anisotropic Electromagnetic Measurements

Jörn Zimmerling*, Vladimir Druskin^{†‡}, Sofia Davydycheva[‡], Wardana Saputra[§], Carlos Torres-Verdín[§], Frank Antonsen[¶], Jon Kåre Lotsberg[¶], and Michael Rabinovich[∥]

ABSTRACT

We develop a new, efficient, and accurate method to simulate frequency-domain borehole electromagnetic (EM) measurements acquired in the presence of three-dimensional (3D) variations of the anisotropic subsurface conductivity. The method is based on solving the quasi-static Maxwell equations with a goal-oriented finite-volume discretization via blockquadrature reduced-order modeling. Discretization is performed with a Lebedev grid that enables accurate and conservative solutions in the presence of any form of anisotropic electrical conductivity. Likewise, the method makes use of a new effective-medium approximation to locally account for non-conformal boundaries and large contrasts in electrical conductivity, especially in the vicinity of EM sources and receivers. The finitevolume discretization yields a large symmetric linear system of equations, which is reduced to a set of smaller structured problems via block Lanczos recursion. The formulation also enables the efficient calculation of the adjoint solution, which is necessary for gradient-based inversion of the measurements to estimate the associated spatial distribution of electrical conductivity, i.e., to solve the inverse problem. Specific applications and verifications of the new numerical simulation algorithm are considered for the case of borehole ultra-deep azimuthal resistivity measurements (UDAR) typically used for subsurface well geosteering and navigation. We verify the efficiency, robustness, and scalability of this approach using synthetic UDAR measurements acquired in a 3D formation inspired by North-Sea geology. The numerical experiments successfully verify the applicability of our modeling approach to real-time UDAR processing frameworks.

INTRODUCTION

Electromagnetic (EM) modeling plays a central role in geophysical imaging, where accurate and efficient forward solvers are essential for inversion-based interpretation of remote-sensing measurements. In the frequency domain, and under the quasi-static approximation in the presence of non-magnetic materials (neglecting displacement currents and assuming that magnetic permeability is a scalar constant μ_0), Maxwell's equations for the electric field can be recast into a second-order partial differential equation. Specifically, the governing partial differential equation for the electric field $\mathcal{E}(\mathbf{x}, \omega)$ is given by

$$(\nabla \times \mu_0^{-1} \nabla \times + i \omega \underline{\underline{\sigma}}(\mathbf{x})) \mathcal{E}(\mathbf{x}, \omega) = -i \omega \mathcal{J}^{\text{ext}}(\mathbf{x}),$$

where $\underline{\underline{\sigma}}(\mathbf{x})$ is the symmetric positive definite 3×3 conductivity tensor, ω is the angular frequency**, $\mathcal{J}^{\mathrm{ext}}(\mathbf{x})$ denotes an externally applied transmitter current density, and \imath denotes the imaginary unit. The right-hand side of the above equation is fully controlled by the user to interrogate the subsurface. Generally, $\mathbf{x} \in \mathbb{R}^3$ is part of an unbounded domain, and we impose amplitude decay conditions at infinity on $\mathcal{E}(\mathbf{x},\omega)$.

The purpose of geophysical EM imaging is to obtain information about the conductivity tensor $\underline{\underline{\sigma}}(\mathbf{x})$ and its spatial distribution in the subsurface from local measurements of the electric field $\mathcal{E}(\mathbf{x},\omega)$ or the magnetic field $-(\imath\omega\mu_0)^{-1}\nabla\times\mathcal{E}(\mathbf{x},\omega)$ at multiple receiver positions \mathbf{x}_r ,

^{. *} Department of Information Technology, Regementsvägen 10, Uppsala University, Sweden; (jorn.zimmerling@uu.it.se).

[†] Worcester Polytechnic Institute and Southern Methodist University, USA.

[‡] 3DEM Holding, USA; (sdavyd@3DEMholding.com).

[§] Hildebrand Department of Petroleum and Geosystems Engineering, The University of Texas at Austin, Austin, USA.

[¶] Equinor.

bp, P&O Subsurface, bp America, Houston, Texas.

^{**.} $\exp(-i\omega t)$ convention in the Fourier transform

over multiple frequencies ω_k and for various transmitter– receiver polarizations. We denote such measurements as samples of the form $\mathcal{E}(\mathbf{x}_r, \omega_k)$, collected for a set of userdefined transmitter locations and polarizations.

The associated forward problem consists of evaluating the electric field at the receiver locations and frequencies given a conductivity model $\underline{\underline{\sigma}}(\mathbf{x})$ and a set of transmitters. Formally,

$$\left(\underline{\underline{\sigma}}(\mathbf{x}), \mathcal{J}_s^{\text{ext}}\right) \mapsto^{\mathbb{F}} \left\{ \mathcal{E}(\mathbf{x}_r, \omega_k; \mathcal{J}_s^{\text{ext}}) \right\}$$
 (1)

where \mathbb{F} denotes the forward modeling operator, $\{\mathbf{x}_r\}$ are the receiver positions, $\{\omega_k\}$ are the interrogation frequencies, and $\{\mathcal{J}_s^{\text{ext}}\}$ are the enabled transmitters (with position and polarization). The corresponding *inverse problem* seeks to estimate the spatial distribution of the conductivity tensor $\sigma(\mathbf{x})$ from these measurements.

In this paper, we focus our attention to borehole Ultra-Deep Azimuthal Resistivity (UDAR) measurements, a modality widely used in logging-while-drilling (LWD) applications and well geosteering (i.e., well navigation). In typical UDAR surveys, triaxial resistivity tools are employed, consisting of three orthogonal transmitter polarizations combined with one or more receiver locations that record all three components of the magnetic field. Such multi-polarization configurations are essential to estimate the full conductivity tensor $\sigma(\mathbf{x})$ of the formation as well as to detect 2D or 3D variations of electrical conductivity. The frequency content used in UDAR applications commonly ranges from approximately 2 kHz up to 96 kHz, enabling depth-of-detection vs. resolution trade-offs that are critical in subsurface well navigation. What differentiates UDAR from other low-frequency borehole measurements is the large separation between transmitters and receivers compared to the bulk skin depth, making it essentially a far-field method. Although our presentation is tailored to the UDAR case, the numerical simulation method described in this paper is equally applicable to other controlled-source electromagnetic modalities such as CSEM, in particular in the far-field regime.

A forward solver suitable for this class of problems must satisfy several key objectives. It must deliver accuracy, with high fidelity and tunable tolerances; preserve fundamental physics, such as reciprocity; and achieve sufficient efficiency to enable real-time inversion on modern computational accelerators. In addition, it should exhibit strong scalability for large 3D problems, provide differentiability through rapid Jacobian computation for gradient-based inversion, and maintain generality so that a single framework can approach 2D and 3D problems in hierarchical inversion workflows. In this paper, we present a forward modeling algorithm that simultaneously achieves the above objectives in the UDAR setting. We call this algorithm targeted because it approximates the measurements $\mathcal{E}(\mathbf{x}_r, \omega_k; \mathcal{J}_s^{\text{ext}})$ without computing the field everywhere.

There is a substantial body of literature about algorithms for geophysical EM forward problems and their associated direct and iterative solvers (see, e.g., Avdeev

(2005); Haber (2014); Grayver and Streich (2012); Pardo et al. (2021) and the references therein). In this work, we focus on the so-called reduced-order model (ROM) approaches, which are particularly well suited for largescale EM problems in geophysics. The central idea of ROM methods in this context is to construct a small-scale (reduced) problem that accurately approximates the EM measurements in large-scale formations—hence the name. Such reduced problems can then be solved efficiently using direct methods, which, due to their poor scalability, are otherwise impractical for large-scale systems. The first method of this class of EM modeling problems was the Spectral Lanczos Decomposition Method (SLDM), introduced in Druskin and Knizhnerman (1988)(a review can be found in Hoerdt et al. (1992), where the authors analyze the long-offset transient electromagnetic (LOTEM) method, which may be regarded as the surface time-domain analogue of UDAR). This approach solved many practical problems previously considered intractable and enabled reliable medium-scale 3D EM simulations as early as in the late 1980s.

In geophysical inversion, the subsurface formation is typically unknown, and the ease and speed of constructing finite-difference (FD) operators often outweigh any accuracy advantages offered by finite-element methods (FEM) (e.g., Pardo et al. (2021)), especially when combined with robust effective-medium approximations based on Kirchhoff's law. Such an effective-medium construction was advanced in Moskow et al. (1999) and Davydycheva and Druskin (1999) to incorporate fully anisotropic conductivities. Moreover, this discretization scheme can be efficiently truncated by introducing optimal exterior coarsening (e.g., Ingerman et al. (2000)), effectively simulating an unbounded domain.

While such discretizations are efficient, they also inherit certain challenges intrinsic to diffusive EM modeling. One of the fundamental obstacles in this regime is the presence of a divergence-free null space of the operator in equation 1, which leads to spurious potential modes at low frequencies. Traditionally, this difficulty has been mitigated using vector-potential formulations (e.g., Haber (2014)) with divergence-free gauge conditions, albeit at the cost of increasing both the size and fill-in of the discretized Maxwell system.

The SLDM addresses the above problem by truncating the spurious modes through a spectral correction at a comparatively low computational cost. This, in turn, enables the use of conservative FD schemes on non-uniform Cartesian grids following Lebedev's formulation in Lebedev (1964), which is equivalent to a finite-volume (FV) formulation. A better-known special case of such a discretized formulation is Yee's scheme from Yee (1966). In this paper, the electric-field formulation was chosen, however, due to the preservation of orthogonality relationships in the discrete operators (Lebedev (1964)); this formulation can be equivalently transformed to a magnetic-field formulation (and vice versa) without any loss of accuracy.

Thus, the particular choice of formulation is of no consequence.

The SLDM has several limitations. Its convergence can be erratic in the presence of large conductivity contrasts, as shown in Saputra et al. (2025). Further, no tight stopping criterion exists for SLDM, it is severely memory—bandwidth-bound on modern computational hardware, and it lacks efficient preconditioners. To address these difficulties, ROM approaches based on rational Krylov subspaces have been proposed as alternatives to SLDM (e.g., Druskin et al. (1999); Zimmerling et al. (2018); Qiu et al. (2019)), proving competitive for late-time controlled-source EM (CSEM) and other near-zone acquisition methods, though less suitable for far-zone methods.

In this paper, we introduce a new ROM framework addressing the above shortcomings which is tailored to modeling and inversion of UDAR measurements in large-scale formation models. The first essential feature of the framework is its two-scale structure, the second is a novel solver based on a goal-oriented block-quadrature approach.

In the two-scale approach, a finely pixelated formation model is represented on a large-scale (potentially irregular) grid and contains billions of nodes in industrial applications. This model is projected onto a tool-centered Cartesian simulation grid using millions of nodes. The simulation grid moves with the tool along realistic 3D curvilinear trajectories. A projection is performed using a novel effective-medium framework, which extracts optimal averaging directions for Kirchhoff's law, corresponding to the principal direction of conductivity-tensor variation within each FV cell computed via the principal component analysis, treating the finely pixelized model as the data. This approach is important in pixel-based inversion, when formation boundaries are not sharply defined or are non-layered, unlike in the layered parameterization used in Davydycheva et al. (2003). The two-scale structure can be traced back to the so-called integro-interpolation methods developed in the 1950s in the former Soviet Union for nuclear physics simulations. Some elements of such a two-scale model were later implemented in the original SLDM code written at the Central Geophysical Expedition, see Hoerdt et al. (1992).

The second essential component for efficient large-scale automated simulation is a robust and scalable Krylov ROM algorithm based on block-quadratures. This approach builds on recent work in Zimmerling et al. (2025); Druskin and Zimmerling (2025), with preliminary applications to UDAR modeling reported in Davydycheva et al. (2023); Saputra et al. (2024, 2025). Block quadrature is a goal-oriented algorithm designed to accurately approximate the multi-input/multi-output (MIMO) transfer function (the EM responses at receiver locations), achieving significantly faster and more stable convergence than SLDM, which computes solutions at all grid points. From the block-quadrature perspective, we derive block-Gauss and block-Gauss-Radau quadratures optimized for far-zone, multi-component electromagnetic arrays.

Compared to the SLDM, the block-quadrature approach has several advantages. Averaging Gauss and Gauss-Radau quadrature rules reduces the approximation error by an order of magnitude at no computational cost, while their difference yields a tight error bound that serves as a reliable stopping criterion; an improvement over SLDM, where termination was often based on ad-hoc self-convergence tests. The block-quadrature is also better aligned with modern computer architectures, which demand higher arithmetic intensity than classical Krylov methods offer, to not be limited by memory bandwidth. In addition, SLDM does not converge monotonically and can behave erratically for hard cases as shown in Saputra et al. (2025), while the quadrature exhibits monotonic convergence, which is also faster and more stable for spurious modes. Finally, the block formulation enables efficient computation of the Jacobian matrix and preserves reciprocity.

METHOD

Below, we show how the discretization of the governing equation leads to a linear system of the form

$$(D + \imath \omega M)\widehat{e} = -\imath \omega j_{x/y/z}^{tx},$$

where D and M are discrete curl-curl and mass/medium operators, respectively, and \widehat{e} is the discretization of the electrical field strength. For the discretization of the operator in equation , we adopt a Lebedev FD scheme, although any mimetic discretization that preserves self-adjointness could be employed for that purpose. In the UDAR setting, multiple tool positions provide multiple transmitter-receiver locations needed for reliable inversion. To obtain accurate UDAR responses from coarsegrid discretizations, the conductivity tensor $\underline{\sigma}$ must be averaged onto the computation grid. New averaging formulas that trade off accurate homogenization with fast computations are also introduced in this section.

After discussing discretization and effective medium averaging, we formulate the computation of the UDAR transfer function as one of block-quadrature. This offers several advantages over methods previously used in the literature. One of these advantages is its ability to compute both fields and adjoint fields, enabling adjoint-based Jacobian computation for gradient-based inversion, which is discussed next. Finally, we introduce our two-geometry model that accommodates curvilinear well trajectories, transforming a global conductivity model into local tool-centered representations at each logging point.

Discretization

In this section, we briefly show how the discretization with N degrees of freedom of the quasi-magnetostatic Maxwell equation leads to the linear system

$$(D + i\omega M)\hat{e} = -i\omega j_{y/y/z}^{tx},$$

where D and M are discrete curl-curl and mass/medium operators, respectively, and $j_{x/y/z}^{tx}$ is the external forcing

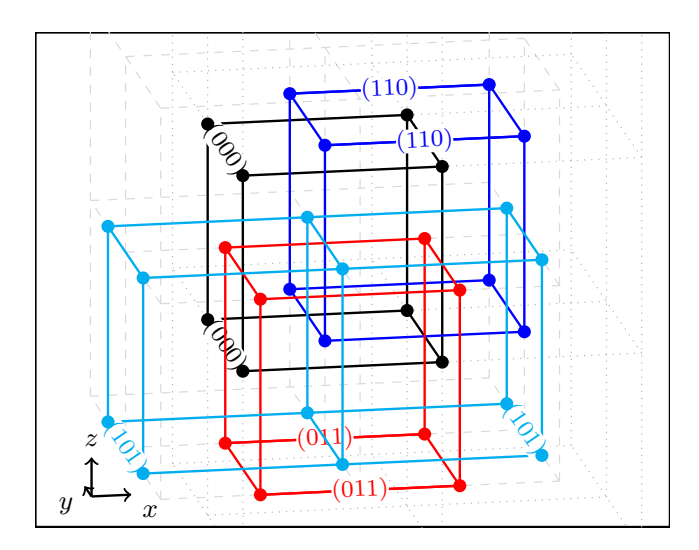


Figure 1: 3D view of the 4 Lebedev clusters shifted in space. Dotted gray lines are the primary grids and dashed gray lines the dual grid.

current density, and \hat{e} is a vector containing the numerical approximation of the electrical field strength.

We use a discretization of the Maxwell operator based on Lebedev's scheme (e.g., Lebedev (1964)). Standard conservative Yee grids from Yee (1966) are incompatible with anisotropic media because the electric field components are defined on the edges of a Yee cube and are therefore not collocated, which prevents the direct application of tensorial conductivity properties. A Lebedev discretization overcomes this limitation by combining four shifted Yee grids, referred to as clusters, as illustrated in Figure 1. Each cluster is identified by a three-bit binary index (000), (011), (101), and (110), where a "1" in a given position indicates a shift along the corresponding axis. Within each cluster, the electric field components are discretized along the edges, as in a conventional Yee grid. By selecting the clusters whose index sum is even, one obtains a consistent Lebedev grid, in which each set of three clusters intersects orthogonally at specific points in space. At these collocation points, all three components of the electric field are defined, allowing the full tensorial medium properties to be applied for accurate modeling.

In summary, each Lebedev cluster supports Yee-grid-style FD differentiation, while the collocation points enable the treatment of fully anisotropic media. The resulting FD scheme remains conservative, preserving key vector identities and physical properties such as current conservation in every elementary cell, as well as symmetry under EM duality transformations (i.e., interchanging the electric and magnetic fields, see Asvadurov et al. (2007)). The clusters can be grouped into pairs with discretization errors of opposite sign, so their averaging leads to partial error cancellation. To fully exploit this property, the discrete transmitter and receiver current densities (denoted as $j^{\text{tx}}_{\text{Y}/\text{Z}}$ and $j^{\text{rx}}_{\text{Y}/\text{Z}}$, respectively) are distributed with equal

weight over all four Lebedev clusters surrounding the corresponding transmitters and receivers. In UDAR applications, these densities are typically normalized to unit magnetic moments. This discretization enables a reduction of the size of the grid compared to the standard Yee grid, even for isotropic media.

Near the well, we typically employ uniform FD spacing, whereas at domain boundaries, optimal geometric grid coarsening is used (see Ingerman et al. (2000)) to simulate an infinite domain and discretize the exterior problem. The choice of grid spacing and the minimal distance to the geometrically coarsened grid are based on the skin depth relevant to the investigation. Before discretization, we non-dimensionalize the Maxwell equations to ensure that the average eigenvalue of the pencil (D,M) is of order $\mathcal{O}(1)$, hence preventing underflow or overflow issues in floating-point arithmetic when solving the resulting system of equations.

Using such a FD scheme, M is block-diagonal and can be efficiently factorized as $M=M^{\frac{1}{2}}M^{\frac{1}{2}}$ and inverted. The transfer function from transmitters to receivers can be written in terms of the symmetric positive semi-definite matrix

$$A = M^{-\frac{1}{2}} D M^{-\frac{1}{2}} \in \mathbb{R}^{N \times N},$$

namely, the Lebedev-approximation of the self-adjoint operator $\underline{\underline{\sigma}}^{-\frac{1}{2}}\nabla\times\mu_0^{-1}\nabla\times\underline{\underline{\sigma}}^{-\frac{1}{2}}$. For example, the transfer function describing the coupling from a z-polarized transmitter $j_z^{\rm tx}$ to an x-polarized receiver $j_x^{\rm tx}$ is given by

$$f_{x;z}^{\mathrm{r;t}}(\omega) = -\imath \omega \left(M^{-\frac{1}{2}} j_x^{\mathrm{rx}} \right)^T (A + \imath \omega I)^{-1} M^{-\frac{1}{2}} j_z^{\mathrm{tx}}. \tag{2}$$

In UDAR systems with three transmitters and three receivers, nine of such couplings need to be computed for every logging point and receiver spacing. In the next section, we discuss how to average conductivities to the FD grid to obtain accurate couplings even on coarse grids. We then show that all nine couplings can be efficiently computed using a block formulation.

Effective media averaging

Using a conservative FD scheme in strongly heterogeneous rock formations requires careful conductivity homogenization in each grid cell, especially when the grid does not align with sharp material interfaces (i.e., non grid-conforming media boundaries). The first SLDM code (MAXWELL) from Druskin and Knizhnerman (1988) assumed that conductivity varied locally in a 1D manner along the coordinate axes. This assumption allowed the computation of effective transversely isotropic (TI) FD conductivities using Kirchhoff's circuit laws, representing the heterogeneous medium as a combination of series and parallel circuits of elementary resistors*. To consider tilted interfaces, Moskow et al. (1999) proposed layering in arbitrary directions within each cell, producing effective fully

^{*.} This approach originated in the unpublished Central Geophysical Expedition (CGE) report by Alexander Kronrod and Alexander Lavut, 1979.

anisotropic FD conductivity tensors. However, their homogenization formulas were computationally expensive in cases of internal cross-bedding (such as in eolian or fluvial sandstones, for instance) and, more importantly, required prior knowledge of the effective direction of 1D variation (hereafter referred to simply as the "effective direction"), which can be difficult to determine in finely pixelated formations derived from EM or other imaging methods.

Consider the cell Ω containing (sub-grid) nodes $\mathbf{x}_i \in \Omega$ of the finely pixelated formation grid, with tensor conductivities $\underline{\sigma}(\mathbf{x}_i) = \underline{\sigma}_i$ for $i = 1, \ldots, n_i^{\text{sub}}$.

For simplicity, we begin with a scalar (isotropic) conductivity function, interpolated in Ω as $\sigma^{\rm iso}(\mathbf{x})$. To determine the effective direction in a data-driven manner, treating the pixelated model as data, we use the representation

$$\nabla \times \nabla \times \mathcal{E} = -\Delta \mathcal{E} - \nabla \left(\mathbf{c} \cdot \mathcal{E} \right), \tag{3}$$

where $\mathbf{c} = \nabla \log(\sigma^{\text{iso}})$. Here, for simplicity, we omit the explicit dependence on space and frequency. We also use the divergence-free condition for the electric field, namely,

$$\nabla \cdot (\sigma^{\text{iso}} \mathcal{E}) = 0.$$

The last term on the right-hand side of equation 3, commonly referred to as the static term, is responsible for spatial discontinuities of $\mathcal{E}(\mathbf{x},\omega)$. We aim to identify a (row) unit vector $\mathbf{k}=(k_x,k_y,k_z)$ with $\|\mathbf{k}\|=1$, representing the effective direction in a finite-volume cell, such that the static term can be approximated via

$$\sigma^{\rm iso}(\mathbf{x}) \approx \sigma(\mathbf{k} \cdot \mathbf{x}),$$

where $\sigma(\cdot)$ is a function of one variable, representing conductivity in an equivalent layered medium in the cell. The vector \mathbf{k} is the principal component of $\nabla \log \sigma^{\mathrm{iso}}(\mathbf{x})$ in the cell, representing the dominant direction of variation. This component can be computed as the dominant right singular vector of the singular value decomposition (SVD) of the matrix $\mathbf{\Gamma} \in \mathbb{R}^{n_i^{\mathrm{sub}} \times 3}$ with the rows $\nabla \log \sigma^{\mathrm{iso}}(\mathbf{x}_i)$.

Let \mathbf{k}_1 and \mathbf{k}_2 form an orthonormal basis in the plane orthogonal to \mathbf{k} , so that \mathbf{k} , \mathbf{k}_1 , and \mathbf{k}_2 form an orthonormal basis in \mathbb{R}^3 . Let

$$\hat{\sigma} = \frac{|\Omega|}{\int_{\Omega} \left[\sigma^{\text{iso}}(\mathbf{x})\right]^{-1} d\Omega} \text{ and } \bar{\sigma} = \frac{\int_{\Omega} \sigma^{\text{iso}}(\mathbf{x}) d\Omega}{|\Omega|}$$

be the harmonic and arithmetic averages, respectively, of the interpolated conductivity in the cell. The harmonic average represents a series circuit (of conductors) along the effective direction, while the arithmetic average represents a parallel circuit along the orthogonal directions. The equivalent finite-difference tensor Σ is then defined as

$$\Sigma = \mathbf{k}^T \hat{\sigma} \mathbf{k} + \mathbf{k}_1^T \bar{\sigma} \mathbf{k}_1 + \mathbf{k}_2^T \bar{\sigma} \mathbf{k}_2, \tag{4}$$

where \cdot^T denotes the transpose.

For anisotropic media, i.e., when $\underline{\underline{\sigma}}(\mathbf{x})$ is a 3×3 symmetric positive-definite matrix-valued function, equation 3 can

		$j_x^{ m tx}$	$j_y^{ m tx}$	$j_z^{ m tx}$	$j_x^{ m rx}$	$j_y^{ m rx}$	$j_z^{ m rx}$	$j_z^{ m rx}$
	$j_x^{ m tx}$	$f_{x;x}^{\mathrm{t;t}}$	$f_{x;y}^{\mathrm{t;t}}$	$f_{x;z}^{\mathrm{t;t}}$	$f_{x;x}^{\mathrm{t;r}}$	$f_{x;y}^{\mathrm{t;r}}$	$f_{x;z}^{\mathrm{t;r}}$	↑
	$j_y^{ m tx}$	$f_{y;x}^{\mathrm{t;t}}$	$f_{y;y}^{\mathrm{t;t}}$	$f_{y;z}^{\mathrm{t;t}}$	$f_{y;x}^{\mathrm{t;r}}$	$f_{y;y}^{\mathrm{t;r}}$	$f_{y;z}^{\mathrm{t;r}}$	j_x^{rx}
$\mathcal{F} =$	$j_z^{ m tx}$	$f_{z;x}^{\mathrm{t;t}}$	$f_{z;y}^{\mathrm{t;t}}$	$f_{z;z}^{\mathrm{t;t}}$	$f_{z;x}^{\mathrm{t;r}}$	$f_{z;y}^{\mathrm{t;r}}$	$f_{z;z}^{ m t;r}$	
	j_x^{rx}	$f_{x;x}^{\mathrm{r;t}}$	$f_{x;y}^{\mathrm{r;t}}$	$f_{x;z}^{\mathrm{r;t}}$	$f_{x;x}^{\mathrm{r;r}}$	$f_{x;y}^{r;r}$	$f_{x;z}^{\mathrm{r;r}}$	$j_z^{ m tx}$
	$j_y^{ m rx}$	$f_{y;x}^{\mathrm{r;t}}$	$f_{y;y}^{\mathrm{r;t}}$	$f_{y;z}^{\mathrm{r;t}}$	$f_{y;x}^{\mathrm{r;r}}$	$f_{y;y}^{r;r}$	$f_{y;z}^{r;r}$	↑
	j_z^{rx}	$f_{z;x}^{\mathrm{r;t}}$	$f_{z;y}^{\mathrm{r;t}}$	$f_{z;z}^{\mathrm{r;t}}$	$f_{z;x}^{\mathrm{r;r}}$	$f_{z;y}^{\mathrm{r;r}}$	$f_{z;z}^{\mathrm{r;r}}$	j_x^{tx}

Figure 2: Left: Block-transfer functions \mathcal{F} , including the nine UDAR coupling components. Right: 3D UDAR measurement system visualizing the three transmitter and receiver current densities.

be approximately[†] extended to define \mathbf{k} , as the principal component of the distribution of ∇ trace[log $\underline{\underline{\sigma}}(\mathbf{x})$] in the cell, replacing the scalar $\nabla \log \sigma^{\text{iso}}(\mathbf{x})$ in the isotropic case.

Analogously to equation 4, we obtain the cross-bedding averaging formula

$$\Sigma = \mathbf{k}^T \mathbf{k} \,\hat{\Sigma} \,\mathbf{k}^T \mathbf{k} + \mathbf{k}_1^T \mathbf{k}_1 \,\bar{\Sigma} \,\mathbf{k}_1^T \mathbf{k}_1 + \mathbf{k}_2^T \mathbf{k}_2 \,\bar{\Sigma} \,\mathbf{k}_2^T \mathbf{k}_2,$$

where \mathbf{k}_1 and \mathbf{k}_2 are as defined above, and $\hat{\Sigma}$ and $\bar{\Sigma}$ are the harmonic (series) and arithmetic (parallel) tensorial averages, respectively, of the interpolated matrix-valued conductivity $\underline{\sigma}(\mathbf{x})$ in Ω . Except for the SVD computation of \mathbf{k}_1 in formula 4, this is known in homogenization theory (e.g., Moskow et al. (1999)). Formula is algebraically equivalent to the standard homogenization of layered cross-bedded anisotropic media described in the latter paper; however, its matrix expression, more suitable for high-performance computing (HPC) implementations, appears to be new.

Block-quadrature formulation

UDAR's directional triaxial measurements usually require all nine measurement couplings (see equation 2) for a given transmitter-receiver separation, i.e., $f_{x;x}^{r;t}, f_{x;y}^{r;t}, \dots$ as shown in the measurement configuration on the right side in Figure 2. At the same time, for gradient-type inversion algorithms, we need to compute Jacobians via an adjoint formulation, which requires computing electrical fields on the entire grid for all direct and reciprocal transmitters (i.e., when the receiver dipole acts as a transmitter). The Jacobian calculation does not need to be as accurate as the measurement coupling, since a moderate error in the Jacobian may only slightly slow down convergence of iterative gradient-based inversion without affecting the final result. Therefore, unlike in the classical SLDM algorithm, we combine all necessary direct and reciprocal solutions for every spacing in one computation, and calculate the UDAR block-transfer function as

$$\mathcal{F}(\omega) = -i\omega B^{T} (A + i\omega I)^{-1} B \in \mathbb{C}^{6 \times 6}, \tag{5}$$

^{†.} These formulas are approximations, since generally $\nabla \log(\underline{\underline{\sigma}}) \neq \underline{\underline{\sigma}}^{-1} \nabla \underline{\underline{\sigma}}$ and $\operatorname{trace}(\underline{\underline{\sigma}} \nabla \mathcal{E}) \neq \nabla \cdot \mathcal{E} \sum_{i,j=1}^{3} \underline{\underline{\sigma}}_{ij}$.

i.e., a 6×6 complex symmetric matrix containing all measured 9 couplings from transmitters $j_{x/y/z}^{\text{tx}}$ to all receivers $j_{x/y/z}^{\text{rx}}$, which are stacked in the block matrix

$$B = M^{-\frac{1}{2}} [j_x^{\text{tx}}, j_y^{\text{tx}}, j_z^{\text{tx}}, j_x^{\text{rx}}, j_y^{\text{rx}}, j_z^{\text{rx}}].$$
 (6)

By construction, thanks to symmetry of A in Lebedev's discretization and symmetric block-representation in equation 5 it satisfies reciprocity $f_{x;y}^{\rm t,r}=f_{x;y}^{\rm r,t}$ as indicated by the color coding in Figure 2. The figure shows that the relevant couplings can be found in the off-diagonal 3×3 block and that the diagonal blocks contain couplings from transmitters and receivers to themselves (e.g. $f^{\rm t,t}$), which are irrelevant. This formulation recasts the problem as an approximation problem for a block-quadratic form as shown in Zimmerling et al. (2025). This recasting is strictly goal-oriented, i.e., we are only interested in finding accurate transfer functions rather than having a good field approximation in the entire domain.

We use a block-Krylov subspace projection of the matrix A onto the space of block-polynomials with degree strictly less than m, i.e.,

$$\{ \pi(A)B : \deg(\pi) < m \},\$$

where π is an ordinary polynomial (e.g., $\pi(z) = c_0 + c_1 z + \cdots + c_{m-1} z^{m-1}$) evaluated at the matrix A. The block size p denotes the number of columns of B and is determined by the number of direct and reciprocal transmitters. In UDAR applications, it is p = 6 if a single spacing is simulated and p = 9 for two spacings in the same simulation.

Let the columns of $\mathbf{Q}_m = [Q_1, \dots, Q_m] \in \mathbb{R}^{N \times pm}$ contain an orthonormal $(\mathbf{Q}_m^T \mathbf{Q}_m = I)$ basis for the block Krylov subspace

$$\mathcal{K}_m(A,B) = \text{blkspan}\{B,AB,\ldots,A^{m-1}B\}.$$

This subspace can be computed via the block Lanczos iteration, which can be compactly written as

$$A\mathbf{Q}_m := \mathbf{Q}_m T_m + Q_{m+1} \boldsymbol{\beta}_{m+1} E_m^T, \tag{7}$$

with T_m symmetric positive definite. The block Lanczos iteration is shown in Algorithm 1. Here, we denote by $E_m \in \mathbb{R}^{N \times p}$ the canonical block basis vector that is all zeros except for the last $p \times p$ block, which is an identity matrix. In the algorithm, bold Greek letters α/β represent $p \times p$ matrices, so-called block-coefficients and all capital letters except A are matrices of the size of the block starting vector B, i.e. $N \times p$.

The approximation of the block-transfer function from equation 5 on the Krylov subspace reads

$$\mathcal{F} \approx \mathcal{F}_m^{\text{Gauss}} = -\imath \omega \boldsymbol{\beta}_1^T E_1^T (T_m + \imath \omega I)^{-1} E_1 \boldsymbol{\beta}_1 \qquad (8)$$

where $E_1 = [I_{p \times p}, 0, \dots, 0]^T$ is the first canonical block basis vector

The block coefficients α_i and β_i are not uniquely determined by the block Lanczos algorithm, because the decomposition of the Gram matrix $W^TW = \beta_i^T\beta_i$ is unique

only up to an orthogonal transformation. We choose β_i to be upper triangular, such that the orthogonalization of $W = Q_i \beta_i$ can be computed via a thin-QR factorization or QR via Cholesky. We recommend full QR factorization if Jacobians need to be computed and QR via Cholesky to reduce computational time if only responses \mathcal{F} are needed. With this choice, T_m is a banded matrix with bandwidth p and $\mathcal{F}_m^{\text{Gauss}}$ and can be efficiently computed using complex banded solvers (e.g. ZGBSV).

For certain operators associated with uniform measures, the non-block version of the algorithm coincides with the classical Gaussian quadrature used to approximate integrals. The block extensions of this formulation via the block Lanczos algorithm then lead to block-Gauss-quadrature (e.g., Golub and Meurant (2010)). Adding p quadrature points at zero by modifying the last block diagonal element to $\hat{\alpha}_m = \alpha_m + \Delta \alpha_m$ leads to a block-Gauss-Radau quadrature approximation $\widehat{\mathcal{F}}_m^{\text{GR}}$ given by

$$\widehat{\mathcal{F}}_{m}^{GR} = -i\omega \boldsymbol{\beta}_{1}^{T} E_{1}^{T} (T_{m} + E_{m} \Delta \boldsymbol{\alpha}_{m} E_{m}^{T} + i\omega I)^{-1} E_{1} \boldsymbol{\beta}_{1}.$$

In Zimmerling et al. (2025), it was shown that the difference between the Gauss and Gauss-Radau quadratures $\|\mathcal{F}_m^{\text{Gauss}} - \widehat{\mathcal{F}}_m^{\text{GR}}\|$ is a tight error bound for the approximation error $\|\mathcal{F} - \mathcal{F}_m^{\text{Gauss}}\|$, which we use as a stopping criterion of the block Lanczos iterations. Further, it was shown that averaged quadrature rules $\frac{1}{2}[\mathcal{F}_m^{\text{Gauss}} - \widehat{\mathcal{F}}_m^{\text{GR}}]$ lead to a one order of magnitude reduction in the approximation error. Additional computational advances incorporating the continuous nature of the spectrum of the Maxwell operator in unbounded domains are discussed in Druskin and Zimmerling (2025).

Unlike SLDM, the block-Gauss and block-Gauss-Radau approximations preserve EM reciprocity by construction, i.e. \mathcal{F}_m is complex symmetric and thus invariant under swapping transmitter and receiver.

Algorithm 1 Block Lanczos iteration

1: Given m, and $A \in \mathbb{R}^{N \times N}$, $B \in \mathbb{R}^{N \times p}$ 2: Orthonormalize B, as $Q_1 \beta_1 = B$ 3: $W \leftarrow AQ_1$ 4: $\alpha_i \leftarrow Q_1^T W$ 5: $W \leftarrow W - Q_1 \alpha_i$ 6: **for** $i = 2, \dots, m$ **do** 7: Orthonormalize W, such that $Q_i \beta_i = W$ 8: $W \leftarrow AQ_i - Q_{i-1}\beta_i^T$ 9: $\alpha_i \leftarrow Q_i^T W$ 10: $W \leftarrow W - Q_i \alpha_i$ 11: **end for**12: Form $T = \begin{bmatrix} \alpha_1 & \beta_2^T \\ \beta_2 & \alpha_2 & \ddots \\ & \ddots & \ddots & \beta_m^T \end{bmatrix}$

The block-quadrature algorithm generalizes to other matrix functions, i.e., if block time-domain signals are re-

quired, they can be efficiently approximated as

$$B^T \exp(-At)B \approx \boldsymbol{\beta}_1^T E_1^T \exp(-T_m t) E_1 \boldsymbol{\beta}_1$$
.

We stress that the block-quadrature algorithm is an all-atonce algorithm, i.e. it gives a solution for all frequencies ω or all times t with a single run of the algorithm.

Due to round-off errors, spurious curl-free modes may appear in numerical computations. These modes manifest as small, non-physical eigenvalues of T, which must be removed in the SLDM framework via spectral truncation (e.g., Druskin and Knizhnerman (1994)). While this procedure is inexpensive for serial computations, it can become a bottleneck on modern CPUs because of limited parallelization. In contrast, within the quadrature-based approach, even this step becomes unnecessary, since the associated spurious spectral weights, i.e., the residues of $\boldsymbol{\beta}_1^T E_1^T (T_m + \imath \omega I)^{-1} E_1 \boldsymbol{\beta}_1$ as a function of $\imath \omega$, are on the order of machine precision and therefore have a negligible effect.

A drawback of Krylov model reduction, including quadrature-based approaches, is that classical preconditioners cannot be used. However, randomized Nyström-preconditioner approaches show potential (e.g., Chen et al. (2025); Zimmerling et al. (2025)), especially for GPU implementations, and this remains an area of future research.

The block recursion offers several computational advantages over both direct solvers and standard (non-block) Krylov methods. Compared to direct solvers, they are very memory efficient, since only three block vectors need to be stored in memory (about 144 MB per million unknowns). Further, direct solvers have an asymptotic complexity of $\mathcal{O}(N^2)$ for 3D problems and remain computationally intractable for N in the millions of unknowns.

Using FD discretizations, the matrix-block-vector product AQ_i can be implemented in a matrix-free fashion; on modern hardware, this step is memory-bandwidth limited and dominated by loading the averaged conductivities and block vectors. At the same time, the arithmetic intensity of the algorithm is increased by working with block-vector operations rather than individual vector operations as in ordinary Krylov methods (SLDM), which leads to better utilization of current computing systems, which are memory-bandwidth-bound for these algorithms. When pis small, the computational cost is dominated by matrixvector products AQ_i and increases affinely in p. The block method reduces the number of iterations required to reach a given tolerance by more than a factor of two compared to SLDM, and together with averaged quadrature rules and a tight stopping criterion, it significantly accelerates the computations. In the future we plan to accelerate the quadrature solver using a GPU implementation, randomized preconditioners, and Krein-Nudelman approaches to block quadratures (see Druskin and Zimmerling (2025); Karpelin (2025)).

Compared to SLDM, the block-quadrature formulation is numerically more stable, computationally better suited for modern hardware, converges faster, and preserves important properties such as reciprocity exactly, and, as shown in the next section, is suited for adjoint-based computation of Jacobians.

Efficient computation of Jacobians in the self-adjoint formulation via block Lanczos

For gradient-based inversion, we need to compute the sensitivity $\delta \mathcal{F}$ of the measurements \mathcal{F} to perturbations in the conductivity tensor $\delta \underline{\sigma}$. Perturbations in the conductivity model after discretization become perturbations in the medium matrix δM . We use the adjoint-state method (e.g., Plessix (2006)) to compute elements of the Jacobian, which requires the electrical field originating from the transmitters, and the adjoint field caused by the receivers; however, we use the self-adjoint formulation of the Maxwell operator, eliminating the need to solve two separate equations for fields and adjoint fields. The elements of the Jacobian are the sensitivities of the measurements $\delta \mathcal{F}(\omega)$ with respect to perturbations of the material coefficients in the mass/medium matrix δM . A straightforward derivation yields the directional (Fréchet) derivative

$$\delta \mathcal{F}(\omega) = -\omega^2 \left[(A + i\omega I)^{-1} B \right]^T M^{-\frac{1}{2}} \left(\delta M \right) \cdot M^{-\frac{1}{2}} (A + i\omega I)^{-1} B.$$

Because we choose a self-adjoint formulation $(A = A^T)$ of our problem, we observe that $\widehat{E} = -\imath \omega M^{-\frac{1}{2}} (A + \imath \omega I)^{-1} B$ are electric fields[†] and adjoint fields at the same time, leading to succinct Jacobian computation via

$$\delta \mathcal{F}(\omega) = [\widehat{E}(\omega)]^T \delta M \,\widehat{E}(\omega). \tag{9}$$

Computation of these inner products is fast for perturbations δM of small support. The block-quadrature formulation naturally suits itself for adjoint methods, since B contains the transmitters and receivers. Thus, $\widehat{E}(\omega)$ can be approximated in the (scaled) block-Krylov subspace for all transmitters and receivers as

$$\widehat{E}(\omega) \approx \widehat{E}_m^{\text{Gauss}}(\omega) = -\imath \omega M^{-\frac{1}{2}} \mathbf{Q}_m (T_m + \imath \omega I)^{-1} E_1 \boldsymbol{\beta}_1.$$

The above (Gauss) field and adjoint field approximations can again be improved by averaging with Gauss-Radau approximations. Storage of the block Lanczos vectors \mathbf{Q}_m is unfeasible and would negate the memory advantage of these methods; however, $\widehat{E}_m^{\text{Gauss}}(\omega)$ can be computed by running the block Lanczos algorithm twice to expand $\widehat{E}_m^{\text{Gauss}}(\omega)$ in the second run from the known block-expansion coefficients $(T_m + i\omega I)^{-1}E_1\boldsymbol{\beta}_1$, so-called two-pass Lanczos. The computational cost of the Jacobian computation is thus roughly twice the cost of approximating the responses \mathcal{F}_m .

^{‡.} The $\widehat{\cdot}$ is used to visually distinguish the electrical field approximation $\widehat{E}_m^{\text{Gauss}}$ from E_m a block-canonical basis vector

Two-frame coordinate model for well-path and formation mapping

The formation at each point in the 3D space is specified in a global (Earth-related) coordinate system (x, y, z) by the vertical and horizontal resistivities, R_v and R_h , respectively, assuming TI-anisotropy. We allow an arbitrary tilt of the formation anisotropy tensor, with formation dip, θ_f , and azimuth, ϕ_f , by defining the local stratigraphic vertical direction of anisotropy, which may vary spatially. Thus, R_v and R_h need not be strictly aligned with the global vertical and horizontal directions. This representation, consistent with a locally layered medium, is simpler than the most general anisotropic case and avoids the need for full-tensor descriptions in coordinate-transformation equations. Specifically, we parameterize the conductivity at each point with four unknowns, whereas a general symmetric tensor would require six.

The well path through the formation follows a curvilinear trajectory, with position (x_n, y_n, z_n) in a right-handed coordinate system (with the z-axis directed downward, e.g., North-East-Down), and orientation defined by the dip θ_n and azimuth ϕ_n at each logging point n. This path is usually computed using the minimum-curvature method, although such an approach is not strictly necessary (see Figure 6).

Our computational grid is aligned with and centered on the tool, such that a coordinate transformation is performed at each logging point from the global coordinates (x, y, z) to the local coordinates $(x_n^{\text{loc}}, y_n^{\text{loc}}, z_n^{\text{loc}})$ related to the tool. The Lebedev grid, attached to the transmitter and receiver(s), remains identical at each point and moves with the tool along the trajectory through the formation.

The local coordinate frame at each logging point n is tangential to the well path (i.e., aligned with the tool; see Figure 6 on the right). First, the coordinate system is translated to (x_n, y_n, z_n) , then rotated by the azimuth angle ϕ_n in the xy-plane (rotation about the z-axis following the left-hand rule), and finally by the dip angle θ_n in the xz-plane (rotation about the y-axis following the right-hand rule).

It is within this local coordinate frame that the grid is constructed, and the formation properties are sampled and averaged. The formation dip and azimuth, meanwhile, are transformed (at each point in 3D space) to local formation dip $\theta_{\rm f}^{\rm loc}$ and azimuth $\phi_{\rm f}^{\rm loc}$, by compounding the global formation parameters and local coordinate rotations. We transform the spherical coordinates under a two-step rotation. The azimuthal angle $\phi_{\rm f,n}^{\rm loc}$ is computed by combining the original angles $\theta_{\rm f}$ and $\phi_{\rm f}$ with the rotation parameters ϕ_n and θ_n . The angle $\theta_{\rm f,n}^{\rm loc}$ is computed using the same parameters, ensuring that the new angle stays within the valid polar range through the arc-cosine. Together, they give the new spherical angles $(\theta_{\rm f,n}^{\rm loc}, \phi_{\rm f,n}^{\rm loc})$ after the point has been rotated in the xz-plane and then in the xy-plane, given by

$$\begin{split} \theta_{\mathrm{f},n}^{\mathrm{loc}} &= \arccos\!\!\left(\cos(\theta_{\mathrm{f}})\cos(\theta_{n}) - \sin(\theta_{\mathrm{f}})\cos(\phi_{\mathrm{f}} - \phi_{n})\sin(\theta_{n})\right), \\ \phi_{\mathrm{f},n}^{\mathrm{loc}} &= \arctan\!\!\left(\frac{\sin(\theta_{\mathrm{f}})\sin(\phi_{\mathrm{f}} - \phi_{n})}{\sin(\theta_{\mathrm{f}})\cos(\phi_{\mathrm{f}} - \phi_{n})\cos(\theta_{n}) + \cos(\theta_{\mathrm{f}})\sin(\theta_{n})}\right) \end{split}$$

At each Lebedev's grid box, a material averaging of the formation properties is performed, and the averaged conductivity tensor is computed.

Overview of Methods

The main technical contribution of our work is a forward modeling method for EM geophysical surveys, verified in the UDAR setting, that meets the objectives outlined in the introduction. Our approach combines a scalable discretization scheme with accurate effective-medium averaging to minimize grid dimensions. A new, efficient and scalable block-quadrature solver, tailored to UDAR and modern computational hardware, delivers significant speedups while preserving key physics such as reciprocity. It also offers differentiability via an adjoint-based Jacobian framework, enabling gradient-based inversion. Finally, the design of both algorithm and discretization is sufficiently general to accommodate 2D and 3D problems within hierarchical inversion workflows.

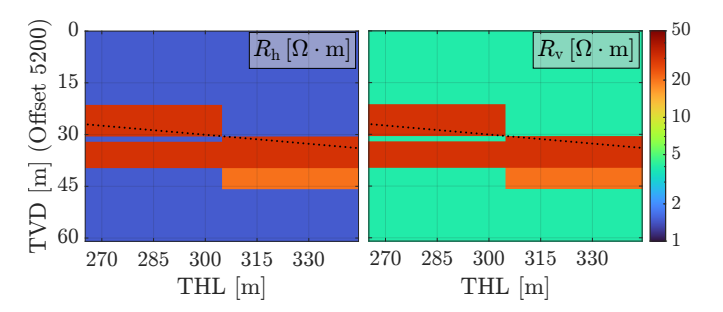


Figure 3: Slice of a layered resistivity model with a fault. The horizontal resistivity, R_h in $[\Omega \cdot m]$, is shown on the left and the vertical resistivity, R_v , on the right.

RESULTS

We present two numerical examples. First, a small-scale 2D example demonstrates the Jacobian computation. Second, a 3D synthetic UDAR experiment in a complex formation is simulated as a self-consistency test. Finally, we discuss the HPC implementation and computational performance at the end of the section.

Jacobian computation

We use a small anisotropic fault model to verify the computation of the Jacobian using the presented solver. Figure 3 (left) shows the horizontal resistivity distribution, while the right shows the vertical resistivity. The configuration is a small section of a larger model starting at a true vertical depth (TVD) of $5.2\,k\mathrm{m}$ and a true horizontal length (THL) of $265\,\mathrm{m}$. The well (dotted line) intersects

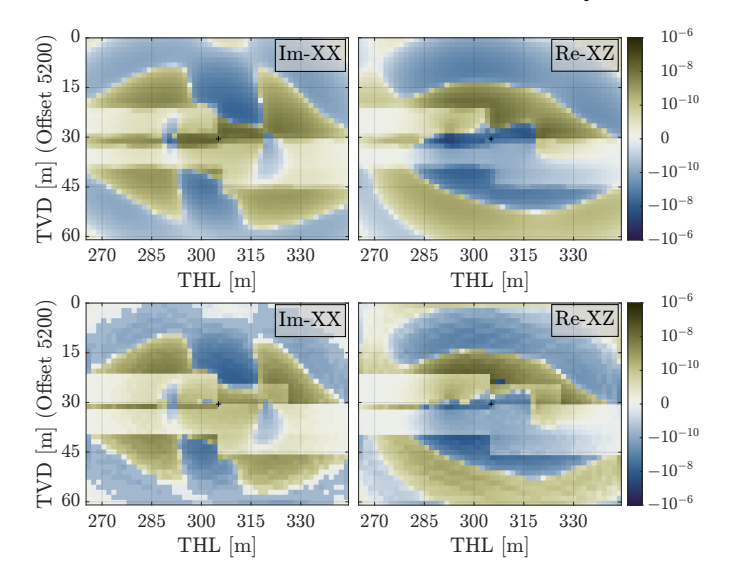


Figure 4: Example components of the adjoint Jacobian computation for R_h (top-row) compared to their FD counterparts (bottom-row).

a vertical fault, with 90° dip and zero azimuth. Although the model is parameterized as a diagonally anisotropic medium, material averaging in a well-centered coordinate system results in full tensorial resistivities. For the synthetic model, we simulate a tool with two receiver spacings of 25.3 and 13.1 m, with operating frequencies of $(6, 12, 24) \, \text{kHz}$ and $(24, 48, 96) \, \text{kHz}$, respectively.

For this simple anisotropic global model consisting of $(52 \times 1 \times 40)$ pixels, with 52 logging points and 6 tool combinations, 1,297,921 forward simulations (n_m+1) are required to calculate the Jacobian using FD differentiation. On a typical desktop computer without parallelization, such a computation would take more than 50 days to complete, making brute-force sensitivity computation infeasible for 2D or 3D inversions. In contrast, using the adjoint method, the sensitivity with respect to $R_{\rm h}$ can be computed in approximately 20 seconds (using an MPI interface to parallelize over logging-point-receiver configurations), representing a substantial reduction in computational cost.

Figures 4 and 5 compare the sensitivities with respect to perturbations in $R_{\rm h}$ and $R_{\rm v}$, respectively. The bottom rows show the corresponding elements of the Jacobian computed via finite-difference differentiation, used to verify our adjoint-based Jacobian formulation. While the method computes sensitivities for all nine couplings and all frequencies simultaneously, for brevity we display here only selected real and imaginary components.

The sensitivities agree well with the finite-difference results showing slight numerical noise. The noise arises from the fact that the transfer function is only locally linear with respect to small perturbations in the medium. For points far from the transmitter and receiver location, this requires numerical tolerances near double precision round-off for accurate finite-difference evaluation.

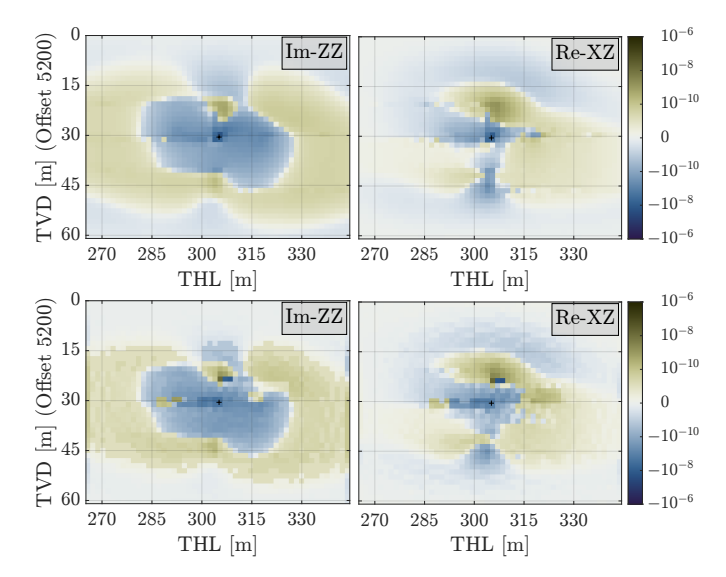


Figure 5: Example components of the Adjoint Jacobian for $R_{\rm v}$ computation (top-row) compared to their FD counterparts (bottom-row).

Measurement example

The developed simulation method was tested and verified by comparing to independent 1D and 3D modeling results (see Saputra et al. (2024, 2025)). Here, we describe a forward-modeling self-consistency test using a challenging 3D synthetic model inspired by field data, as well as an actual field and measurement condition as acquired in the North Sea.

Figure 6 on the left shows a vertical cross-section of the synthetic reservoir model intersected by a curvilinear well trajectory, indicated with a white dotted line in front of the section and a black dotted line behind it. The model represents a rotated and eroded fault block characteristic of North Sea hydrocarbon traps. Reservoir zones, shown in red and yellow, correspond to hydrocarbon-filled formations. The simulated well trajectory is designed to assess the sensitivity of UDAR measurements to fault proximity, evaluating how accurately faults can be mapped for geosteering decisions.

There are a total of 408 logging points along the well trajectory. Figure 6 on the right shows the FD grid attached to the tool's transmitter and receiver, overlaid on the medium cross-section. The grid is generated automatically, with a uniform discretization used between the transmitter and receiver and around the tool. The outer regions are terminated by 10–20 geometrically increasing, spectrally optimal steps to emulate an infinite domain. Typically, between 10 and 20 uniform nodes per minimal skin depth are required for a given model and tool frequency range.

A single run of the forward-modeling algorithm computes all nine magnetic couplings at all tool frequencies for one logging position. Figures 7 and 8 show the synthetic logs at 12 kHz and 48 kHz, respectively. For brevity, only

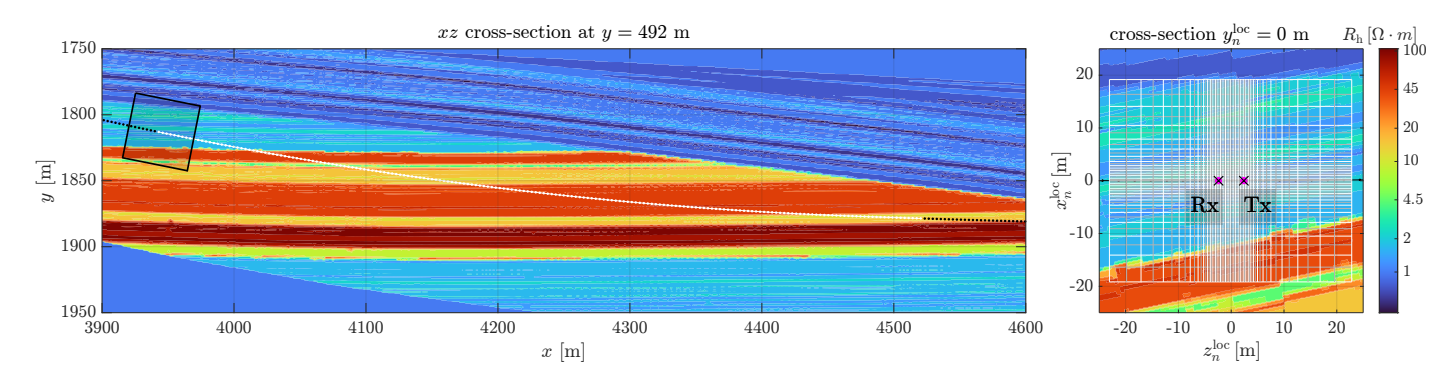


Figure 6: Left: Vertical cross-section of a full 3D synthetic reservoir model with general anisotropy intersected by a curvilinear well trajectory (black and white dotted lines, respectively, behind and in front of the model cross-section). Right: FD grid attached to the tool's transmitter and receiver (black ×), on the background of the 3D medium cross-section (see black shaded rectangle on the left for location). White and gray lines identify primary and dual nodes, respectively, of the Lebedev grid.

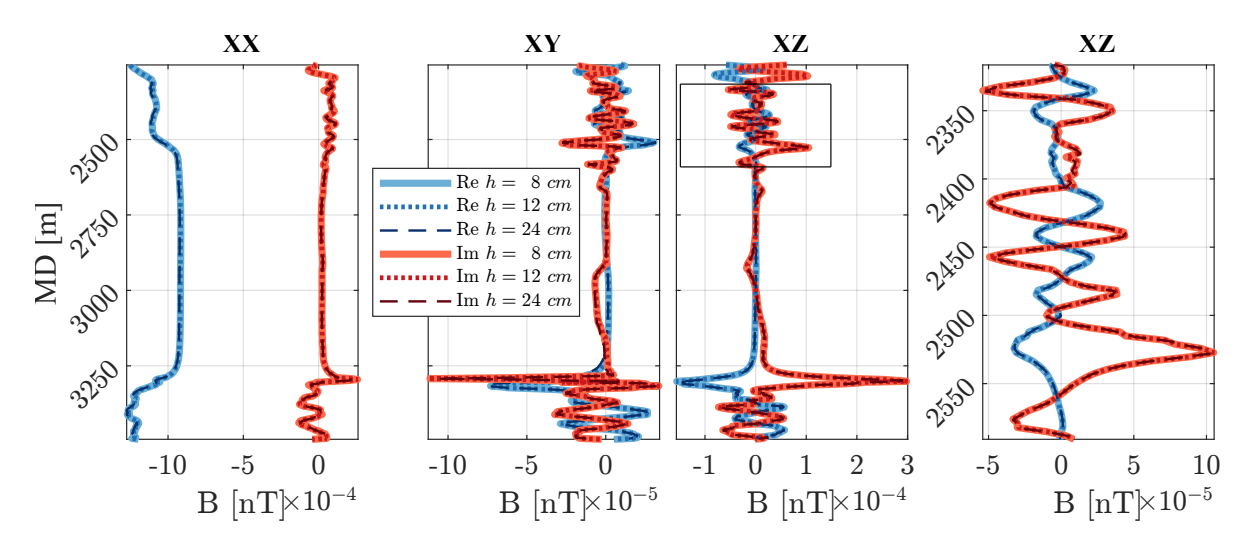


Figure 7: Synthetic UDAR measurements at 12 kHz through the medium described in Figure 6. Displayed are three couplings XX, XY and XZ of the B-fields (real, in blue, and imaginary parts, in red). Solid, dotted and dashed lines correspond to the uniform grid steps of, respectively, 8, 12, and 24 cm. The box in the XZ graph indicates the landing section that is shown with more detail in the right most graph.

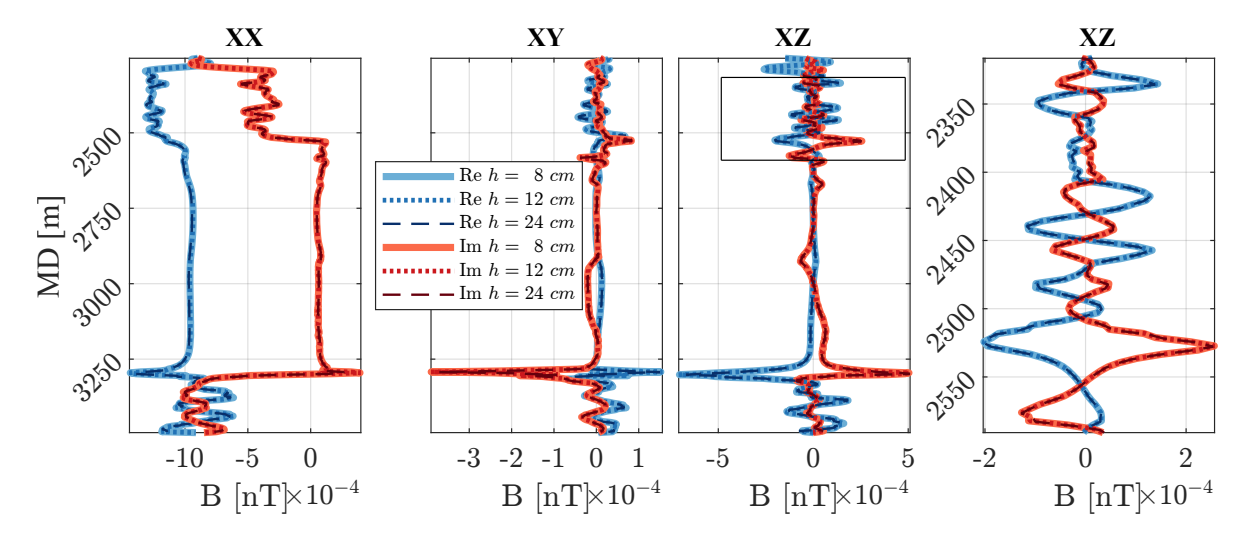


Figure 8: Synthetic UDAR measurements at 48 kHz through the medium described in Figure 6. The landing section, as indicated by the black box, is shown with more detail in the right most graph.

the XX, XY, and XZ couplings are displayed. The left three graphs show the entire set of measurements, while the right-most graph is a zoomed-in view of the landing section (measured depth (MD), $2500-2750\,\mathrm{m}$), indicated by the black box in the top panels. Real and imaginary parts are shown in blue and red, respectively. Solid, dotted, and dashed lines correspond to uniform grid spacings of 8, 12, and 24 cm, respectively.

Minimal and maximal skin depths for the given medium model and frequency range are $1.4\,\mathrm{m}$ and $54\,\mathrm{m}$, respectively. The two finest discretizations agree closely, with only minor discrepancies observed for the coarsest grid. This example verifies that the developed effective-medium formulation accurately captures the EM response even at relatively coarse discretizations.

The three discretizations result in systems of increasing sizes $N_{24\,\mathrm{cm}} = 320 \times 10^3$, $N_{12\,\mathrm{cm}} = 516 \times 10^3$, and $N_{8\,\mathrm{cm}} = 1058 \times 10^3$ unknowns, respectively. Figure 9 describes the the solver convergence for a logging point located within the landing zone. Displayed is the relative error in the UDAR responses corresponding to the off-diagonal 3×3 block of \mathcal{F} . The number of iterations required to reach a given tolerance is approximately inversely proportional to the minimum mesh size, h.

The latter behavior is similar to the SLDM estimate reported in Druskin and Knizhnerman (1989, 1994). However, as shown in Saputra et al. (2025), the proportionality coefficient for the block-Gauss quadrature is significantly improved, and unlike SLDM, its convergence is steady and monotonic. The tightness of the Gauss-Radau error bound motivates its use as a robust stopping criterion, while the combined Gauss/Gauss-Radau averaging yields a substantial reduction in the approximation error. Moreover, potential extensions based on the Krein-Nudelman framework from Druskin and Zimmerling (2025) and Nyström preconditioning from Chen et al. (2025) could further reduce the dependence on the discretization parameter h, particularly for strongly non-uniform meshes.

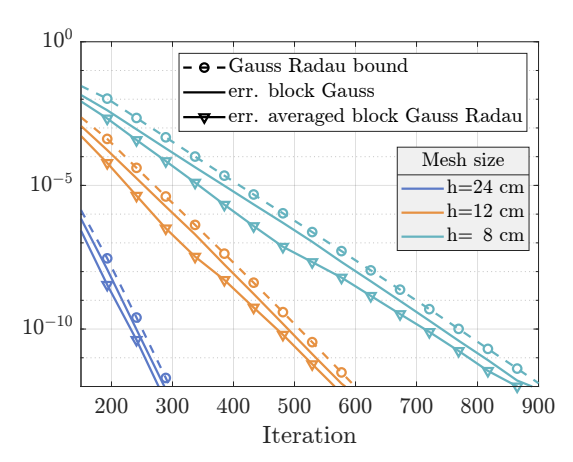


Figure 9: Convergence of the solver for a single logging point in the landing zone for the 3 different mesh sizes.

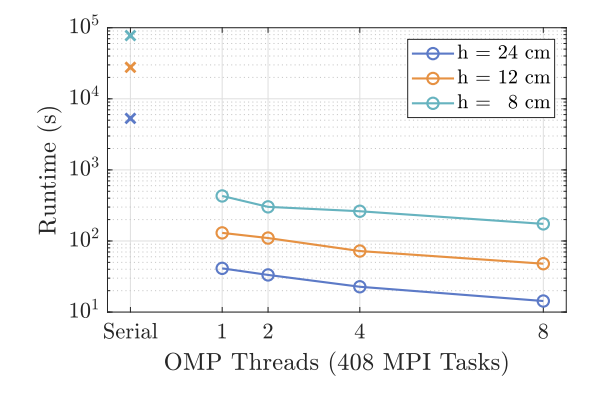


Figure 10: Dependence of (Log-)runtime for the three minimal mesh sizes on the degrees of parallelization. With the increasing number of OMP threads, the number of computing nodes was increased to have one core per thread.

Hybrid OpenMP/MPI Parallelization

To achieve real-time simulation of 3D UDAR measurements, a hybrid OpenMP/MPI parallelization was implemented. The MPI layer is used to launch and distribute multiple simulation tasks corresponding to different logging point-receiver configurations across the available computing resources, with multiple MPI ranks assigned per node. Within each rank, OpenMP (OMP) provides shared-memory parallelism for a single logging point across the available CPU cores. To achieve peak performance, the number of MPI tasks (ranks) should ideally match the total number of independent configurations simulated, i.e., the number of logging points multiplied by the number of receiver spacings. The second parallel region operates at the block-quadrature-solver level using OpenMP, which optimizes numerous linear algebra operations (LAPACK/BLAS).

Table 1 summarizes the total runtimes obtained for 3 different mesh sizes and varying degrees of parallelism. Parallel simulations were executed on the TACC Stampede 3 supercomputer using 408 MPI tasks (one task per logging-point-receiver configuration) with 1, 2, 4, and 8 OpenMP threads per task, using 4, 8, 15, and 30 compute nodes, respectively. Serial runs were performed on a laptop for reference using 12 OpenMP threads. As expected, a consistent reduction in wall-clock time is observed with increasing thread count, as shown in Figure 10. For all mesh resolutions, the runtime decreases by approximately a factor of 2.5 when moving from one to eight OpenMP threads, reflecting the combined effects of memory bandwidth limitations and coordination between OpenMP threads.

The per-logging-point computation time of the serial run is comparable to that of the MPI implementation despite substantial hardware differences, mainly due to scheduling overheads. Furthermore, the logging points in the resistive section converge more slowly, and the MPI implementation is limited by the slowest logging point. In

min.	P	$\mathbf{Serial}^{\dagger}$			
Mesh	408 MPI	Run			
Size	1 OMP	2 OMP	4 OMP	8 OMP	Time(s)
h = 24 cm	41.2	33.3	22.7	14.3	5,304
h = 12 cm	130	110	72.2	47.9	27,744
h = 8 cm	430	302	262	174	77,520

- ‡ Supercomputer: TACC Stampede 3 (Saphire Rapid).
- † Personal laptop: Intel® Core™ Ultra 7 165U (1.70 GHz) 12 OMP threads

Table 1: Runtime comparison showing strong scaling for different minimum mesh sizes and parallel configurations for the full UDAR measurements containing 408 logging points. Parallel runs were performed on dual-socket Intel[®] Xeon[®] CPU Max 9480 (Sapphire Rapids) nodes on TACC Stampede 3, each with 112 cores per node. Runs with 4, 8, 15, and 30 nodes were configured with 1, 2, 4, and 8 OpenMP threads per MPI task, respectively.

future work, we plan to make the OpenMP thread count dependent on the expected computational cost of a given logging point. In this hybrid OpenMP/MPI framework, the speedup scales almost linearly with the number of MPI tasks but not with OpenMP threads. Therefore, when the number of cores is limited, increasing the number of MPI tasks should be prioritized over increasing the number of OpenMP threads.

CONCLUSIONS

We developed, implemented, and verified a new goal-oriented ROM framework specifically targeted for far-zone EM measurements, such as borehole UDAR array. The fundamental technical innovation of this approach is treating the problem as block-quadrature targeted to transmitter-receiver coupling simulations rather than EM-field approximation on the entire FD grid. Our new simulation framework builds on the authors' recent contributions, including fully automated heterogeneous media averaging and an accelerated, robust block-quadrature solver optimized for modern HPC architectures. The solver provides tolerance control through quadrature error bounds and enables cost-free error reduction through quadrature averaging.

Moreover, the solver supports the computation of adjointbased Jacobians for gradient-based inversion workflows with only a negligible increase in computational cost. Largescale numerical simulations of a synthetic set of UDAR measurements verified the efficiency, scalability, and competitiveness of the developed approach and its MPI-based HPC implementation. When implemented on massively parallel computers, the algorithm can accurately simulate UDAR measurements acquired along a large-scale 3D anisotropic formation comprising an array of five transmitter-receiver separations, each including nine triaxial couplings and operating at four discrete frequencies. Such a configuration, corresponding to a single logging point along the well trajectory, can be simulated in tens of CPU seconds. For one logging point, the block-quadrature solver is $3 \times$ faster than SLDM at points where SLDM converges well. In spatially complex geological settings, however, SLDM may exhibit erratic behavior and converge slowly, whereas the proposed approach remains robust and converges monotonically.

Future work will focus on improving the averaging scheme to better capture corner effects, thereby enhancing accuracy in complex geological settings and near faults. We also plan to accelerate the quadrature solver using a GPU implementation, randomized preconditioners, and Krein-Nudelman approaches to block quadratures. Preliminary experiments suggest speedups of at least one order of magnitude, bringing real-time 3D inversion of LWD measurements with stochastic uncertainty quantification within reach.

ACKNOWLEDGMENTS

This work was supported by the University of Texas at Austin's Deep Imaging Sub-Consortium (of the Research Consortium on Formation Evaluation), currently sponsored by AkerBP, Baker-Hughes, bp, ENI, Equinor ASA, Halliburton, and Petrobras. The authors also acknowledge the Texas Advanced Computing Center at the University of Texas at Austin for providing HPC resources on Stampede 3.

Carlos Torres-Verdín is thankful for the financial support provided by (a) the Brian James Jennings Endowed Memorial Chair in Petroleum and Geosystems Engineering, and (b) the 2025 Moncrief Grand Challenge Award by the Oden Institute, both from the University of Texas at Austin.

Vladimir Druskin was partially supported by AFOSR grants FA 9550-20-1-0079, FA9550-23-1-0220, and NSF grant DMS-2110773.

REFERENCES

Asvadurov, S., V. Druskin, and S. Moskow, 2007, Optimal grids for anisotropic problems: Electronic Transactions on Numerical Analysis, **26**, 55–81.

Avdeev, D. B., 2005, Three-dimensional electromagnetic modelling and inversion from theory to application: Surveys in Geophysics, **26**, 767–799.

Chen, T., C. Huber, E. Lin, and H. Zaid, 2025, Preconditioning without a preconditioner: faster ridge-regression and gaussian sampling with randomized block Krylov subspace methods.

Davydycheva, S., and V. Druskin, 1999, Staggered grid for Maxwell's equations in 3-D anisotropic media: Threedimensional Electromagnetics, 138.

Davydycheva, S., V. Druskin, and T. Habashy, 2003, An efficient finite-difference scheme for electromagnetic logging in 3D anisotropic inhomogeneous media: Geophysics, **68**, 1525–1536.

Davydycheva, S., C. Torres-Verdín, J. Hou, W. Saputra, M. Rabinovich, F. Antonsen, B. E. Danielsen, V. Druskin, and J. Zimmerling, 2023, 3D electromagnetic modeling and quality control of ultradeep borehole az-

- imuthal resistivity measurements: Presented at the SP-WLA 64th Annual Logging Symposium.
- Druskin, V., and L. Knizhnerman, 1988, A spectral semidiscrete method for numerical solution of 3-D nonstationary problems in electrical prospecting: Phys. Sol. Earth, 24, 641–648.
- ——, 1994, Spectral approach to solving threedimensional Maxwell's diffusion equations in the time and frequency domains: Radio Science, **29**, 937–953.
- Druskin, V., and J. Zimmerling, 2025, A Krylov projection algorithm for large symmetric matrices with dense spectra.
- Druskin, V. L., L. Knizhnerman, and P. Lee, 1999, New spectral Lanczos decomposition method for induction modeling in arbitrary 3-D geometry: Geophysics, 64, 701–706.
- Druskin, V. L., and L. A. Knizhnerman, 1989, Two polynomial methods of calculating functions of symmetric matrices: USSR Computational Mathematics and Mathematical Physics, 29, 112–121.
- Golub, G. H., and G. Meurant, 2010, Matrices, moments, and quadrature with applications: Princeton University Press. Princeton Series in Applied Mathematics.
- Grayver, A., and R. Streich, 2012, in Comparison of iterative and direct solvers for 3D CSEM modeling: seg, 1–6.
- Haber, E., 2014, Computational methods in geophysical electromagnetics: Society for Industrial and Applied Mathematics (SIAM).
- Hoerdt, A., V. L. Druskin, L. A. Knizhnerman, and K.-M. Strack, 1992, Interpretation of 3-D effects in long-offset transient electromagnetic (LOTEM) soundings in the Münsterland area/Germany: Geophysics, 57, 1127–1137
- Ingerman, D., V. Druskin, and L. Knizhnerman, 2000, Optimal finite difference grids and rational approximations of the square root I. Elliptic problems: Communications on Pure and Applied Mathematics, 53, 1039– 1066.
- Karpelin, E., 2025, The fast and the finite-differenced: Optimal block-Lanczos for Lebedev grids on GPUs: Master's thesis, Uppsala University, Sweden.
- Lebedev, V. I., 1964, Difference analogues of orthogonal decompositions of basic differential operators and some boundary value problems. i: Soviet Comput. Math. Math. Phys., 4, 449–465. (in Russian).
- Moskow, S., V. Druskin, T. Habashy, P. Lee, and S. Davydycheva, 1999, A finite difference scheme for elliptic equations with rough coefficients using a cartesian grid nonconforming to interfaces: SIAM Journal on Numerical Analysis, **36**, 442–464.
- Pardo, D., P. J. Matuszyk, V. Puzyrev, C. Torres-Verdin, M. J. Nam, and V. M. Calo, 2021, Modeling of resistivity and acoustic borehole logging measurements using finite element methods, 1st ed.: Elsevier.
- Plessix, R.-E., 2006, A review of the adjoint-state method for computing the gradient of a functional with geophys-

- ical applications: Geophysical Journal International, **167**, 495–503.
- Qiu, C., S. Güttel, X. Ren, C. Yin, Y. Liu, B. Zhang, and G. Egbert, 2019, A block rational Krylov method for 3-D time-domain marine controlled-source electromagnetic modelling: Geophysical Journal International, 218, 100–114.
- Saputra, W., J. Ambia, C. Torres-Verdín, S. Davydycheva, V. Druskin, and J. Zimmerling, 2024, Adaptive multidimensional inversion for borehole ultra-deep azimuthal resistivity: Presented at the SPWLA 65th Annual Logging Symposium. (Conference Paper).
- Saputra, W., C. Torres-Verdín, J. Ambia, B. G. Klappauf, W. Zhan, N. Jahani, J. Zimmerling, V. Druskin, S. Davydycheva, I. Davydychev, and E. R. Fjeldberg, 2025, Recent developments and verifications for the multi-dimensional and data-adaptive interpretation of borehole UDAR measurements: Presented at the SP-WLA 66th Annual Logging Symposium. (Conference Paper).
- Yee, K. S., 1966, Numerical solution of initial boundary value problems involving Maxwell's equations in isotropic media: IEEE Transactions on Antennas and Propagation, 14, 302–307.
- Zimmerling, J., V. Druskin, and V. Simoncini, 2025, Monotonicity, bounds and acceleration of block Gauss and Gauss–Radau quadrature for computing: Journal of Scientific Computing, 103.
- Zimmerling, J., V. Druskin, M. Zaslavsky, and R. F. Remis, 2018, Model-order reduction of electromagnetic fields in open domains: Geophysics, 83, WB61–WB70.